RSC Advances

PAPER

View Article Online
View Journal | View Issue

Cite this: *RSC Adv.*, 2023, **13**, 9441

Theoretical and experimental comparison of the performance of gold, titanium, and platinum nanodiscs as contrast agents for photoacoustic imaging

Jung-Sub Wi, [a] Jiwoong Kim,[b] Myeong Yun Kim, [c] Seongwook Choi, [b] Hae Jue Jung,[c] Chulhong Kim [*b] and Hee-Kyung Na [*c]

Exogenous contrast agents in photoacoustic imaging help improve spatial resolution and penetration depth and enable targeted molecular imaging. To screen efficient photoacoustic signaling materials as contrast agents, we propose a light absorption-weighted figure of merit (FOM) that can be calculated using material data from the literature and numerically simulated light absorption cross-sections. The calculated light absorption-weighted FOM shows that a Ti nanodisc has a photoacoustic conversion performance similar to that of an Au nanodisc and better than that of a Pt nanodisc. The photoacoustic imaging results of Ti, Au, and Pt nanodiscs, which are physically synthesized with identical shapes and dimensions, experimentally demonstrated that the Ti nanodisc could be a highly efficient contrast agent.

Received 6th February 2023
Accepted 13th March 2023

DOI: 10.1039/d3ra00795b

rsc.li/rsc-advances

Introduction

Photoacoustic imaging (PAI), which has the working principle of converting light energy into sound waves, is being studied for use in preclinical and clinical areas due to several advantages, such as a deep imaging depth, high spatial resolution, a wide field of view, and high contrast.[1–10] These distinct advantages of PAI enable applications in cancer detection and staging, whole-body imaging of small animals, and full-ocular imaging of large animals.[11–15] Despite its advantages, PAI has limitations that need to be addressed. One major challenge of PAI is its limited depth of penetration, which is determined by the wavelength of the laser used and typically ranges from a few millimeters to a few centimeters.[16–19] This limitation may make it unsuitable for imaging deeper structures or organs. Another limitation is its sensitivity to tissue heterogeneity, particularly in tissues with high levels of fat or water, which can absorb or scatter light and reduce image quality. In addition, the presence of blood vessels and other structures can also affect image accuracy. To overcome these limitations, exogenous contrast agents, particularly nanoparticles designed for effective nonradiative conversion of the incident near-infrared (NIR) light, have gained significant interest in PAI due to their unique optical and physical properties, enabling them to penetrate deeper into tissues and generate high-resolution images.[16,19–27] Among various exogenous contrast agents, gold nanoparticles have large light absorption cross-sections resulting from the light-induced collective oscillation of electrons in the nanoparticles, namely a localized surface plasmon resonance (LSPR).[28,29] Besides the effective light absorption, gold nanoparticles are known to be biocompatible and their surfaces can be easily modified with well-developed thiol chemistry.[30–32] Although gold nanoparticles have several merits, gold is a scarce element in Earth's crust. Moreover, the relatively low melting temperature of gold compared to other metals becomes much lower depending on the size of the nanoparticle,[33,34] which is why the shape of gold nanoparticles are easily deformed when irradiated with light.[35–37] Intense light pulses transform high-aspect-ratio gold nanostructures, such as nanorods and nanostars, into spherical nanoparticles, and even spherical gold nanoparticles can also be fragmented and reconstituted by light.[25,38,39] In this regard, research has been conducted to develop nano-material based photoacoustic contrast agents such as titanium nitride or platinum.[40] However, it has been difficult to accurately compare the performance and characteristics of these contrast agents due to differences in their shape and size. To propose a contrast agent for PAI that is more abundant than gold and more stable when irradiated, in this report, the theoretical photoacoustic conversion performances of candidate materials were calculated using basic material data and numerically simulated absorption cross-sections. Then, the photoacoustic conversion performances were experimentally confirmed using physically

[a]*Department of Materials Science and Engineering, Hanbat National University, Daejeon 34158, Republic of Korea*

[b]*Departments of Electrical Engineering, Convergence IT Engineering, and Mechanical Engineering, School of Interdisciplinary Bioscience and Bioengineering, Medical Device Innovation Center, Pohang University of Science and Technology, Pohang 37673, Republic of Korea. E-mail: chulhong@postech.edu*

[c]*Safety Measurement Institute, Korea Research Institute of Standards and Science, Daejeon 34113, Republic of Korea. E-mail: nahk@kriss.re.kr*

synthesized metal nanodiscs with identical dimensions and different materials.

Experimental

Electromagnetic simulation

The extinction and absorption cross-sections of the metal nanodiscs were calculated using three-dimensional finite-difference time-domain (FDTD) software (ANSYS Lumerical FDTD). Total-field-scattered field (TFSF) light was used as a light source to separate the computational volume into two distinct regions for the calculations of scattering and absorption cross-sections. The mesh size of the simulation was set to a 1.0 nm cubic grid, and the dielectric properties of Au, Ti, and Pt from Palik's results (data included in the software) were used for the simulation. The nanodiscs in a uniform dielectric medium ($n = 1.33$) were illuminated from the top with a linearly polarized plane wave from the TFSF source.

Physical synthesis of metal nanodiscs

The physical synthesis of the metal nanodiscs using nanoimprinting lithography and vacuum deposition has been described in previous reports.[41–43] Although the amount of nanodiscs synthesized is limited by the lithographic pattern density (typically 5×10^{10} per 4-inch-scale wafer), physical synthesis enables a reproducible and reliable control of nanodisc dimensions.[41–43] In brief, two polymer layers, nanoimprint resist (mr-I 8020R; Microresist Technology, Germany) and sacrificial layer (PMGI-SF3; MicroChem, Japan), were spin-coated onto a Si substrate on which a 100 nm thick Al film was deposited. Then, a nanohole array with a diameter of 160 nm and a period of 300 nm was patterned on the mr-I 8020R layer by thermal nanoimprint lithography. After nanoimprinting, the residual nanoimprint resist at the bottom of the nanohole was dry-etched using O_2 plasma. The PMGI-SF3 layer was dissolved using a wet etchant (AZ 300 MIF; AZ Electronic Materials, USA) to form an undercut profile. Using a thermal evaporator, Au, Pt, or Ti thin film was deposited with a thickness of 20 nm. For the case of Au nanodisc, the dimensions of 160 nm diameter and 20 nm thickness make it resonate with near-infrared (NIR) light suitable for PAI.[42] After the deposition, the mr-I 8020R and PMGI-SF3 layers were removed with a film remover (Remover PG; MicroChem, Japan) to leave only the metal nanodiscs deposited inside the nanohole patterns. After the fabrication of the metal nanodiscs, the final step involved the removal of the Al layer, which was used as a sacrificial layer during the fabrication process. This removal process was necessary to release the metal nanodiscs from the wafer surface. The chosen method for the removal of the Al layer was the use of a 1 wt% trisodium citrate dihydrate solution. Trisodium citrate dihydrate solution is a mild reagent that can selectively dissolve the aluminum layer without affecting the metal nanodiscs. The dissolution process was carried out by immersing the sample in the trisodium citrate dihydrate solution for 10 minutes in a bath sonicator at 60 °C. Afterward, the sample was repeatedly washed with deionized water to remove any residual trisodium citrate dihydrate solution and collected by centrifugation. The molar concentration of 40 pM (corresponding to approximately 2.4×10^{10} nanodiscs per mL) was calculated from the metal concentration measured by inductively coupled plasma atomic emission spectroscopy (PerkinElmer, OPTIMA 7300 DV) and the dimensions of metal nanodiscs. The nanodiscs were characterized by scanning electron microscopy (Hitachi S-4800, Japan), transmission electron microscopy (JEOL JEM-2100F, Japan), and ultraviolet-visible spectroscopy (UV-2600, Shimadzu, Japan).

Measurement of photoacoustic signal amplitudes

For PAI and quantification of photoacoustic signal amplitudes, the previously developed photoacoustic computed tomography system was used.[44,45] A tunable optical parametric oscillator laser system (PhotoSonus M-20, Ekspla, Inc., Lithuania; 20 Hz repetition frequency) irradiated a target to induce photoacoustic signal. The generated photoacoustic signal was detected by a 1024-elements hemispherical ultrasound transducer array (Japan Probe, Inc., Japan) and processed through a data acquisition system (Vantage256, Verasonics, Inc., USA). To obtain photoacoustic spectra, we imaged the silicone tube containing solutions with 750, 760, 770, 780, 790, 800, 810, 820, 830, 850, 900 and 950 nm wavelengths. After capturing a region of a tube as a polygon in a maximum amplitude projection image, the pixel values within the region were arranged in descending order and the mean of the top 1–30% values were considered to represent each solution's photoacoustic signal.[46] Averaging the photoacoustic signals of all pixels within a specific region of interest can lead to overshooting values and noise. To minimize this, the representative photoacoustic signal, namely the mean of the top 1–30% photoacoustic signal, was used. The mean photoacoustic value was normalized to the incident laser energy for each wavelength measured with an energy meter (ES220C, Thorlabs, Inc., USA) to compensate for the difference in laser energy.

Results and discussion

To assess candidate metal nanoparticles as contrast agents for PAI, the optical cross-sections of the nanodiscs were calculated by the three-dimensional FDTD simulation. The two-dimensional (2D) nanodiscs considered in this study are more advantageous for the random incidence and polarization of light than the one-dimensional (1D) nanorods due to their shape isotrop.[42,47,48] For this reason, the molar extinction coefficients of 2D nanodiscs are typically 10-times larger than those of 1D nanorods.[42] Fig. 1 shows the numerically calculated extinction and absorption cross sections of Ti, Pt, and Au nanodiscs with the same diameter of 160 nm and a thickness of 20 nm. To mimic an aqueous solution of nanodiscs, it was assumed that the nanodiscs were surrounded by a medium with a constant refractive index of 1.33. As shown in Fig. 1, when compared to the Ti and Pt nanodiscs, the extinction curve of the Au nanodisc exhibited typical LSPR behavior accompanying a specific wavelength dependence and had the largest extinction

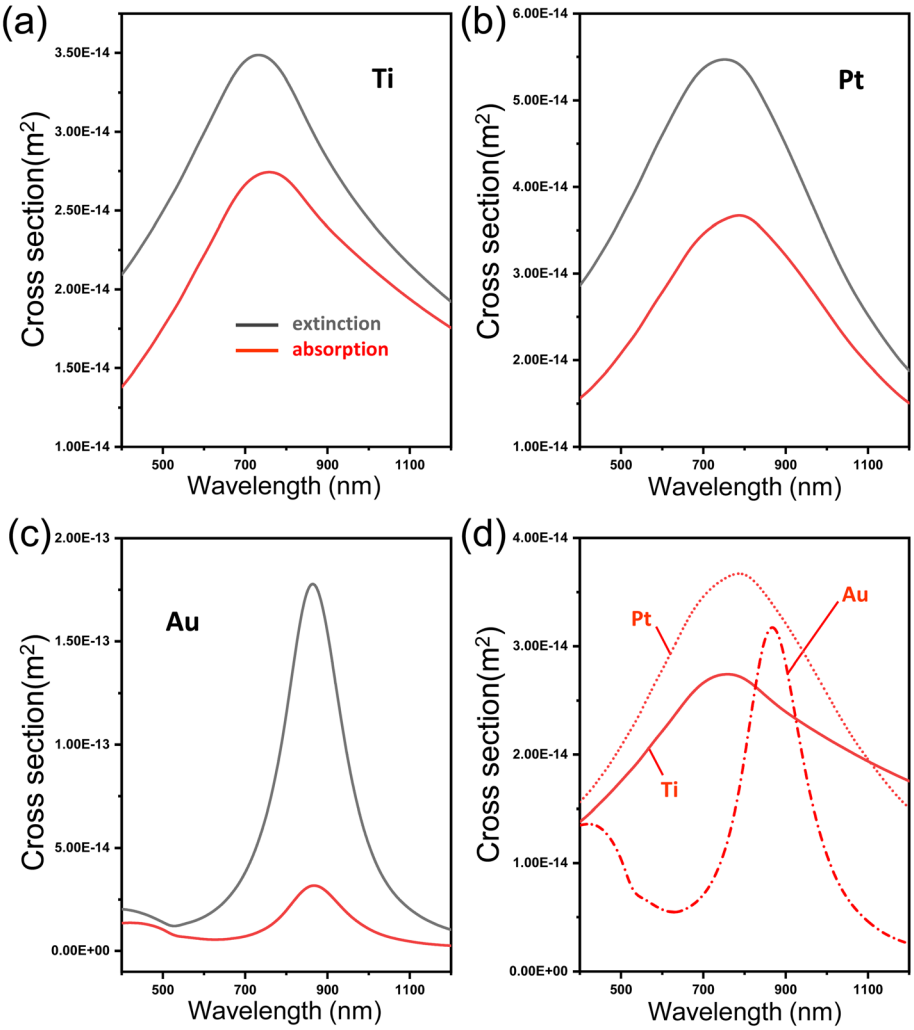

Fig. 1 Numerically simulated extinction (black line) and absorption (red line) spectra of (a) Ti, (b) Pt, and (c) Au nanodisc. The diameter and thickness of Ti, Pt, and Au nanodiscs are all 160 nm and 20 nm, respectively. (d) Simulated absorption spectra of Ti (solid line), Pt (dotted line), and Au (dash-dot line) nanodiscs. The direction of incident light and its polarization angle were perpendicular and parallel to the diameter direction of the nanodisc, respectively.

cross-section. It is noteworthy that all three types of nanodiscs showed optical resonances in the NIR window. Interestingly, the absorption cross-section of the Ti nanodisc is comparable to that of well-known plasmonic nanodiscs of Au and Pt.

Along with the light absorption capability shown in Fig. 1, the relative thermal expansion with the surrounding medium, such as water, and the photoacoustic wave transmission into the medium should be considered together for efficient photoacoustic conversion. Lee *et al.* defined figure-of-merit (FOM) for photoacoustic generation with the equation by

$$\mathrm{FOM} = \frac{\Gamma}{\Gamma_\mathrm{W}} \times T_\mathrm{W}$$

where $\Gamma = \beta c^2/C_\mathrm{p}$ is the Grüneisen parameter (β = volumetric thermal expansion coefficient, c = sound speed, C_p = specific heat capacity at constant pressure), Γ_W is the Grüneisen parameter of water, and T_W is acoustic transmission into water.[49] T_W is given by

$$T_\mathrm{W} = \frac{2Z_\mathrm{W}}{Z + Z_\mathrm{W}}$$

where Z is the acoustic impedance ($Z = \rho c$, ρ is the mass density) and Z_W is the impedance of water.[49] Γ/Γ_W and T_W respectively consider how much the light-absorbing material expands relative to water and how efficiently the photoacoustic wave travels across the interface between the light-absorbing material and water. Table 1 summarizes the material properties of the candidate contrast agents: Au, Pt, and Ti nanodiscs. The Au nanodisc showed the largest value of the normalized Grüneisen parameter (Γ/Γ_W), which meant that the thermal expansion of the Au nanodisc was the greatest when the light of the same intensity was absorbed. However, the Au nanodisc was not the best concerning the acoustic impedance to water (T_W). The Ti nanodisc had more than twice the T_W value of the Au nanodisc. For this reason, the Ti nanodisc has the largest FOM for photoacoustic generation, followed by Au nanodisc and Pt nanodisc.

Table 1 Material properties for comparison of photoacoustic efficiency

Metal	Normalized Grüneisen parameter (Γ/Γ_W)	Acoustic impedance to water (T_W)	FOM	Relative light absorption[a]	Absorption-weighted FOM[b]
Au	30.5	0.047	1.43	1	1.43
Pt	19.5	0.042	0.82	1.15	0.94
Ti	16.4	0.104	1.71	0.85	1.45

[a] Normalized to the absorption cross-section of the Au nanodisc. [b] Figure of merit multiplied by the relative light absorption.

In the above FOM equation given by Lee *at al.*,[49] the light absorption cross-section of the target material was not considered, although it is an inherent property of the material. Therefore, for a more practical and direct comparison of absorbing materials, the absorption cross-sections of the nanodiscs presented in Fig. 1(d) can be a weighting factor to be multiplied by the FOM. The relative light absorptions in Table 1 were obtained by normalizing the maximum absorption cross-section of each nanodisc (3.19×10^{-14} m^2 of Au nanodisc, 3.67×10^{-14} m^2 of Pt nanodisc, 2.72×10^{-14} m^2 of Ti nanodisc) with that of the Au nanodisc. The light absorption-weighted FOM, calculated by multiplying the FOM by the relative light absorption, shows that the Ti nanodisc and Au nanodisc exhibit similar photoacoustic conversion performance.

To experimentally demonstrate the photoacoustic conversion performance of the metal nanodiscs, Ti, Pt, and Au nanodiscs were synthesized using a physical method in which the target metals were vacuum-deposited on a lithographically patterned substrate. The diameter and thickness of the metal nanodiscs were independently defined by the lithographic pattern diameter and the deposited film thickness, respectively. An increase in diameter or decrease in thickness induces a redshift of resonant wavelength.[42] The SEM images in Fig. 2 confirm that the three different metal nanodiscs were synthesized with the same diameter and thickness of approximately 160 nm and 20 nm, respectively. The TEM and energy dispersive spectroscopy (EDS) mapping images in Fig. 2 show that those nanodiscs that look identical are each made of different materials. In addition, the measured absorbance spectra of the aqueous solutions of Ti, Pt, and Au nanodiscs in Fig. 3 corresponded with the simulated spectra in Fig. 1. The absorbance spectrum of the Au nanodiscs showed the narrowest curve. All three types of metal nanodiscs had optical resonances in the NIR window between 700 nm and 900 nm. For Ti nanodiscs, the measured resonant wavelength shows a redshift of about 40 nm compared to the simulated one, which is thought to be due to the native TiO_2 surface layer of high refractive index.

Finally, photoacoustic signal amplitudes of the metal nanodiscs were measured in the NIR wavelength window from 750 nm to 900 nm. A 5 ns pulsed laser beam illuminated the aqueous nanodisc solutions in the plastic tubes. The generated photoacoustic signals were detected using ultrasound transducers. Fig. 4(a) shows the photoacoustic spectra obtained from three different metal nanodisc solutions with the same concentration of 40 pM. The overall shapes and peak wavelengths of the photoacoustic spectra corresponded to those of the extinction spectra shown in Fig. 3. Additionally, the maximum photoacoustic signal amplitudes of the nanodiscs exhibited a trend very similar to the absorption-weighted FOM presented in Table 1. The Au and Ti nanodiscs had approximately 1.6 times greater photoacoustic signal amplitudes and 1.5 times greater absorption-weighted FOM than the Pt nanodiscs. The photoacoustic images in Fig. 4(b) were selected at the wavelengths of the maximum signal amplitudes of each

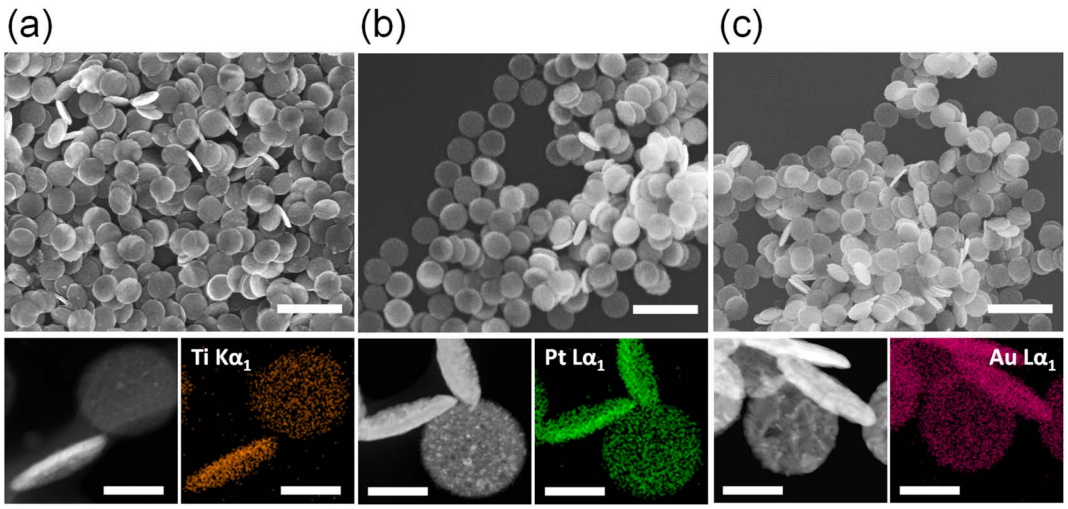

Fig. 2 Electron microscopy analysis results of the (a) Ti, (b) Pt, and (c) Au nanodiscs. Upper panels show SEM images of the nanodiscs. Lower left and right panels show TEM and EDS mapping images, respectively. The scale bars of SEM and TEM images are 400 nm and 100 nm, respectively.

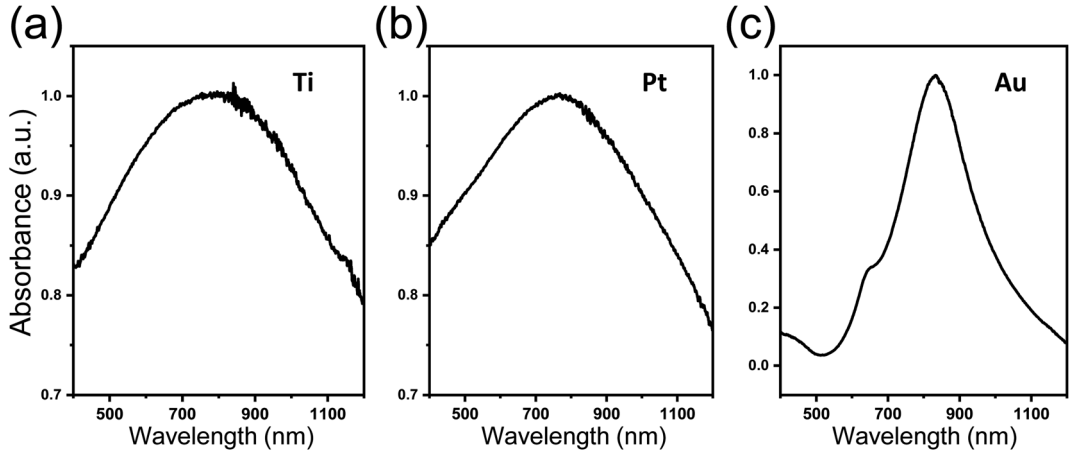

Fig. 3 Measured absorbance spectra of the (a) Ti, (b) Pt, and (c) Au nanodisc solutions. The physically synthesized nanodiscs were dispersed in DI water and the measured spectra were normalized for comparison.

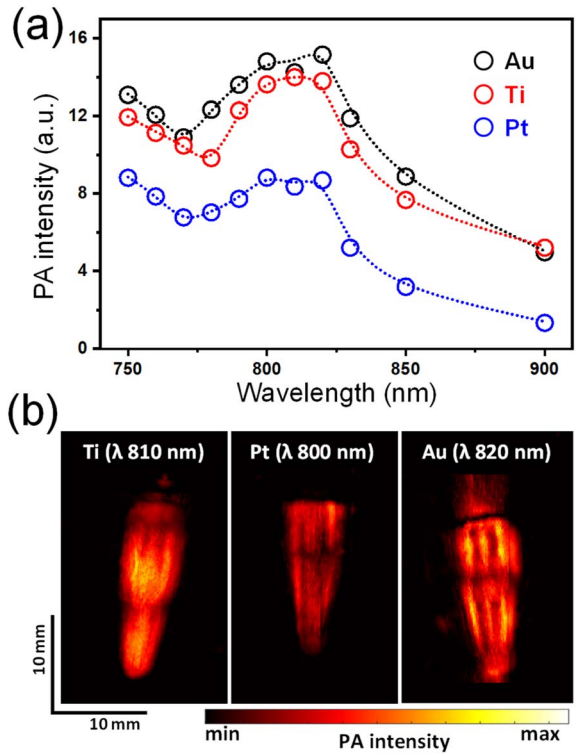

Fig. 4 (a) Photoacoustic spectra of the aqueous solutions of Ti, Pt, and Au nanodiscs having the same concentration of 40 pM. The photoacoustic signals were measured with multiple laser wavelengths from 750 nm to 900 nm and were normalized to their incident laser energies for comparison. (b) Plane-view photoacoustic images of aqueous solutions of Ti, Pt, and Au nanodiscs in centrifuge tubes. The laser wavelengths used for these photoacoustic images (810 nm for Ti, 800 nm for Pt, and 820 nm for Au) corresponded to the peak wavelengths of the photoacoustic spectra shown in Fig. 3(a).

nanodisc, and they visually demonstrated that the photoacoustic conversion performance of the proposed Ti nanodiscs was comparable to that of the Au nanodiscs and superior to that of the Pt nanodiscs. In addition to the fact that Ti has a photoacoustic conversion performance similar to that of Au, Ti is the ninth most abundant element in the Earth's crust and the melting temperature of Ti is approximately 600 K higher than that of Au. Recently, Ti nanostructures have been studied for photothermal or photodynamic therapeutic applications.[50] Therefore, given their abundance in the earth, thermal stability, and photoacoustic conversion performance, Ti nanodiscs have significant advantages as efficient contrast agents for PAI.

Conclusions

To screen candidates for photoacoustic signalling materials, we proposed a light absorption-weighted FOM that can be calculated using their material data in the literature and numerically simulated light absorption cross-sections. Based on the light absorption-weighted FOM, the Ti nanodisc was expected to have a photoacoustic conversion performance similar to that of the Au nanodisc and better than that of the Pt nanodisc. Ti, Au, and Pt nanodiscs with identical shapes and dimensions were successfully synthesized to prove this theoretical expectation. The experimental measurements of the light extinction spectra, photoacoustic spectra, and photoacoustic images of the three candidate materials demonstrated that the Ti nanodiscs could be highly efficient contrast agents for PAI. Considering the present results of photoacoustic conversion performance and other advantages, such as abundance in the earth and thermal stability, we expect that the proposed Ti nanodiscs could become promising exogenous contrast agents for PAI.

Conflicts of interest

There are no conflicts to declare.

Acknowledgements

This research was supported by the research fund of Hanbat National University in 2022 and by National Research Foundation of Korea (grant no. 2019H1A2A1076500, 2020R1A6A1A03047902,

2021M3C1C3097624, 2021R1I1A3048262, 2021M3C1C3097638, 2021RIS-004, 2023R1A2C3004880).

References

1 M. Xu and L. V. Wang, *Rev. Sci. Instrum.*, 2006, **77**, 041101.
2 S. Mallidi, G. P. Luke and S. Emelianov, *Trends Biotechnol.*, 2011, **29**, 213–221.
3 A. B. E. Attia, G. Balasundaram, M. Moothanchery, U. S. Dinish, R. Bi, V. Ntziachristos and M. Olivo, *Photoacoustics*, 2019, **16**, 100144.
4 S. Jeon, J. Kim, D. Lee, J. W. Baik and C. Kim, *Photoacoustics*, 2019, **15**, 100141.
5 B. Park, S. Park, J. Kim and C. Kim, *Adv. Drug Delivery Rev.*, 2022, **184**, 114235.
6 J. Ahn, J. W. Baik, Y. Kim, K. Choi, J. Park, H. Kim, J. Y. Kim, H. H. Kim, S. H. Nam and C. Kim, *Photoacoustics*, 2022, **27**, 100374.
7 W. Choi, E.-Y. Park, S. Jeon, Y. Yang, B. Park, J. Ahn, S. Cho, C. Lee, D.-K. Seo, J.-H. Cho and C. Kim, *Radiology*, 2022, **303**, 467–473.
8 S.-W. Cho, S. M. Park, B. Park, D. Y. Kim, T. G. Lee, B.-M. Kim, C. Kim, J. Kim, S.-W. Lee and C.-S. Kim, *Photoacoustics*, 2021, **24**, 100291.
9 J. W. Baik, H. Kim, M. Son, J. Choi, K. G. Kim, J. H. Baek, Y. H. Park, J. An, H. Y. Choi, S. Y. Ryu, J. Y. Kim, K. Byun and C. Kim, *Laser Photonics Rev.*, 2021, **15**, 2100124.
10 J. Ahn, J. Y. Kim, W. Choi and C. Kim, *Photoacoustics*, 2021, **23**, 100282.
11 A. de la Zerda, Y. M. Paulus, R. Teed, S. Bodapati, Y. Dollberg, B. T. Khuri-Yakub, M. S. Blumenkranz, D. M. Moshfeghi and S. S. Gambhir, *Opt. Lett.*, 2010, **35**, 270–272.
12 J. Xia and L. V. Wang, *IEEE Trans. Biomed. Eng.*, 2014, **61**, 1380–1389.
13 W. Liu and H. F. Zhang, *Photoacoustics*, 2016, **4**, 112–123.
14 O. Liba and A. de la Zerda, *Nat. Biomed. Eng.*, 2017, **1**, 0075.
15 J. Park, B. Park, T. Y. Kim, S. Jung, W. J. Choi, J. Ahn, D. H. Yoon, J. Kim, S. Jeon, D. Lee, U. Yong, J. Jang, W. J. Kim, H. K. Kim, U. Jeong, H. H. Kim and C. Kim, *Proc. Natl. Acad. Sci. U. S. A.*, 2021, **118**, e1920879118.
16 J. Weber, P. C. Beard and S. E. Bohndiek, *Nat. Methods*, 2016, **13**, 639–650.
17 M. Maturi, E. Locatelli, I. Monaco and M. Comes Franchini, *Biomater. Sci.*, 2019, **7**, 1746–1775.
18 S. Wang, J. Lin, T. Wang, X. Chen and P. Huang, *Theranostics*, 2016, **6**, 2394–2413.
19 W. Choi, B. Park, S. Choi, D. Oh, J. Kim and C. Kim, *Chem. Rev.*, 2023, DOI: **10.1021/acs.chemrev.2c00627**.
20 Q. Fu, R. Zhu, J. Song, H. Yang and X. Chen, *Adv. Mater.*, 2019, **31**, 1805875.
21 P. K. Upputuri and M. Pramanik, *Wiley Interdiscip. Rev. Nanomed.*, 2020, **12**, e1618.
22 E.-Y. Park, D. Oh, S. Park, W. Kim and C. Kim, *APL Bioeng.*, 2021, **5**, 031510.
23 A. Karlas, M. Kallmayer, M. Bariotakis, N.-A. Fasoula, E. Liapis, F. Hyafil, J. Pelisek, M. Wildgruber, H.-H. Eckstein and V. Ntziachristos, *Photoacoustics*, 2021, **23**, 100283.
24 K. Cardinell, N. Gupta, B. D. Koivisto, J. C. Kumaradas, X. Zhou, H. Irving, P. Luciani and Y. H. Yücel, *Photoacoustics*, 2021, **21**, 100239.
25 Y. Chen, C. Xu, Y. Cheng and Q. Cheng, *Photoacoustics*, 2021, **23**, 100284.
26 H. I. Kilian, C. Ma, H. Zhang, M. Chen, A. Nilam, B. Quinn, Y. Tang, J. Xia, J. Yao and J. F. Lovell, *Photoacoustics*, 2022, **28**, 100406.
27 J. Vonk, J. Kukačka, P. J. Steinkamp, J. G. de Wit, F. J. Voskuil, W. T. R. Hooghiemstra, M. Bader, D. Jüstel, V. Ntziachristos, G. M. van Dam and M. J. H. Witjes, *Photoacoustics*, 2022, **26**, 100362.
28 E. Hutter and J. H. Fendler, *Adv. Mater.*, 2004, **16**, 1685–1706.
29 K. A. Willets and R. P. V. Duyne, *Annu. Rev. Phys. Chem.*, 2007, **58**, 267–297.
30 E. Boisselier and D. Astruc, *Chem. Soc. Rev.*, 2009, **38**, 1759–1782.
31 A. M. Alkilany and C. J. Murphy, *J. Nanopart. Res.*, 2010, **12**, 2313–2333.
32 Y. Chen, Y. Xianyu and X. Jiang, *Acc. Chem. Res.*, 2017, **50**, 310–319.
33 P. Buffat and J. P. Borel, *Phys. Rev. A: At., Mol., Opt. Phys.*, 1976, **13**, 2287.
34 J.-H. Shim, B.-J. Lee and Y. W. Cho, *Surf. Sci.*, 2002, **512**, 262–268.
35 G. Opletal, G. Grochola, Y. H. Chui, I. K. Snook and S. P. Russo, *J. Phys. Chem. C*, 2011, **115**, 4375–4380.
36 N. Sumimoto, K. Nakao, T. Yamamoto, K. Yasuda, S. Matsumura and Y. Niidome, *Microscopy*, 2014, **63**, 261–268.
37 G. González-Rubio, P. Díaz-Núñez, A. Rivera, A. Prada, G. Tardajos, J. González-Izquierdo, L. Bañares, P. Llombart, L. G. Macdowell, M. Alcolea Palafox, L. M. Liz-Marzán, O. Peña-Rodríguez and A. Guerrero-Martínez, *Science*, 2017, **358**, 640–644.
38 S. Link, C. Burda, B. Nikoobakht and M. A. El-Sayed, *J. Phys. Chem. B*, 2000, **104**, 6152–6163.
39 G. González-Rubio, A. Guerrero-Martínez and L. M. Liz-Marzán, *Acc. Chem. Res.*, 2016, **49**, 678–686.
40 W. He, K. Ai, C. Jiang, Y. Li, X. Song and L. Lu, *Biomaterials*, 2017, **132**, 37–47.
41 J.-S. Wi, E. S. Barnard, R. J. Wilson, M. Zhang, M. Tang, M. L. Brongersma and S. X. Wang, *ACS Nano*, 2011, **5**, 6449–6457.
42 J.-S. Wi, J. Park, H. Kang, D. Jung, S.-W. Lee and T. G. Lee, *ACS Nano*, 2017, **11**, 6225–6232.
43 J. Lee, H.-J. Lee, S.-W. Lee, H.-K. Na, T. G. Lee, J.-S. Wi and S. Kang, *Adv. Photonics Res.*, 2022, **3**, 2100162.
44 J. Yang, S. Choi and C. Kim, *Biomed. Eng. Lett.*, 2022, **12**, 19–35.
45 S. Choi, J. Yang, S. Y. Lee, J. Kim, J. Lee, W. J. Kim, S. Lee and C. Kim, *Adv. Sci.*, 2023, **10**, 2202089.
46 D. Maji, D. Oh, K. Sharmah Gautam, M. Zhou, H. Zhang, J. Kao, D. Giblin, M. Smith, J. Lim, S. Lee, Y. Kang,

W. J. Kim, C. Kim and S. Achilefu, *Analysis Sensing*, 2022, **2**, e202100045.

47 H. B. Song, J.-S. Wi, D. H. Jo, J. H. Kim, S.-W. Lee, T. G. Lee and J. H. Kim, *Nanomedicine*, 2017, **13**, 1901–1911.

48 J. Park, H. Kang, Y. H. Kim, S.-W. Lee, T. G. Lee and J.-S. Wi, *Nanoscale*, 2016, **8**, 15514–15520.

49 T. Lee, H. W. Baac, Q. Li and L. J. Guo, *Adv. Opt. Mater.*, 2018, **6**, 1800491.

50 S. Sargazi, S. Er, S. Sacide Gelen, A. Rahdar, M. Bilal, R. Arshad, N. Ajalli, M. Farhan Ali Khan and S. Pandey, *J. Drug Delivery Sci. Technol.*, 2022, **75**, 103605.